Arch. Metall. Mater. **71** (2026), 1, 387-397

DOI: https://doi.org/10.24425/amm.2026.157801

JIAQI WEN[1,2], CHENGHONG LIU[3,4], ZHIJUN HE[1,2*], LIHUA GAO[1,2*]

SYNTHESIS AND CHARACTERIZATION OF MICRON-SIZED SPHERICAL $MnFe_2O_4$ BY THE OXIDIZATION ROASTING PROCESS

The oxidization roasting process is an effective method for synthetizing micron-sized spherical manganese ferrite ($MnFe_2O_4$) with a multilayer structure. In the synthesis process of the manganese ferrite samples, the phase formation, morphology evolution and interfacial reactions of the MnO-Fe_2O_3 system under different factors were comparatively investigated. The experimental results revealed that manganese ferrite with a magnetization saturation (Ms) value of 64.96 emu/g and a coercivity (Hc) value of 34.10 Oe can be successfully synthesized for 30 min at 1300°C with a Mn/Fe molar ratio of 1:2 in an air atmosphere. However, the micron-sized spherical manganese ferrite samples exhibited a total pore volume of 0.034 cm^3/g, a pore volume of 0.032 cm^3/g, a specific surface area (SSA) of 6.41 cm^3/g and an average particle size (APS) of 20.96 nm. The reduction roasting conditions facilitated the formation of micron-sized spherical $MnFe_2O_4$, with $Fe_xMn_{1-x}O$ ($0 \leq y \leq 1$) as intermediates. These intermediates were subsequently oxidized to $Mn_xFe_{3-x}O_4$ ($1 < x \leq 3$), $Mn_xFe_{3-x}O_4$ ($0 < x < 1$), and $MnFe_2O_4$ under different stages and conditions. Additionally, tetrahedral coordinated Mn^{2+} ions in Mn_3O_4 with spinel-type crystal structures were replaced by tetrahedral coordinated Fe^{2+} ions to form $Mn_xFe_{3-x}O_4$ with a similar crystal structure. Both normal and inverse spinel structures of manganese ferrite coexist and transform during the synthesis of $Mn_xFe_{3-x}O_4$ via the oxidization roasting process.

Keywords: Manganese ferrite; oxidation method; chemical characteristics; oxidation roasting

1. Introduction

Spinel-type manganese ferrites leverage the benefits of iron–manganese composites and serve as effective ferrite materials [1,2]. Owing to its stable spinel-type structure, high saturation magnetization, good biocompatibility and high catalytic activity, manganese ferrite has been commonly used in many fields [3], such as the electronics, environmental protection and biomedical industries [4,5]. Studies have utilized different techniques to synthesize functional manganese ferrite nanocrystals, including hydrometallurgical techniques [6-8], solid-state methods [9], high-energy milling [10,11], and integrated methodologies of pyrometallurgy and hydrometallurgy [12-14]. However, these processes suffer from limited sources of raw materials, relatively complex preparation processes and low yields [15-18]. The proposed scheme can not only meet the requirements of large-scale production and industrial application but also provide a more effective and economical way to synthesize functional materials of iron and manganese oxide.

A range of techniques for the synthesis of micron-sized spherical $MnFe_2O_4$ have been documented, such as solid-state reaction methods [19-21], the salt-assisted solution combustion technique [22], the sol–gel method [23], coprecipitation [24], and hydrometallurgical techniques [25,26]. However, the microscopic morphology of the manganese ferrate products varies on the basis of the different preparation methods employed. Stoia et al. [27] reported that $MnFe_2O_4$ nanoparticles and $MnFe_2O_4$/C nanocomposites were synthesized via a new solvothermal method. As reported, the formed manganese ferrite nanoparticles are unstable during heat treatment in an oxidizing atmosphere owing to Mn(II) oxidation of Mn(III). Ahmed [28] noted that manganese ferrite spinel was synthesized from FeO and MnO via ceramic technology and explored the factors influencing its magnetic and mechanical properties. To conclude, its magnetic and mechanical properties depend not only on the sintering conditions but also on the MnFe molar ratio. Zhang et al. [16] reported that manganese ferrite ($Mn_xFe_{3-x}O_4$) was successfully synthesized in a MnO_2-Fe_2O_3 system. These results demonstrated that the

[1] UNIVERSITY OF SCIENCE AND TECHNOLOGY LIAONING, SCHOOL OF MATERIALS AND METALLURGY, 114051, ANSHAN, LIAONING, CHINA
[2] KEY LABORATORY OF GREEN LOW-CARBON AND INTELLIGENT METALLURGY, LIAONING PROVINCE. 114051, ANSHAN, LIAONING, CHINA
[3] BAOTOU RESEARCH INSTITUTE OF RARE EARTHS, BAOTOU, 014030, INNER MONGOLIA, CHINA

* Corresponding authors: gaolihuaneu@163.com, hzhj2002@126.com

micromorphology of the $Mn_xFe_{3-x}O_4$ particles steadily became more regular with increasing x value. Ultimately, manganese ferrite presented a regular polyhedral structure accompanied by a multilayer stacking structure. As studied by Liu et al. [16], the primary objective of this research is to elucidate the complex interactions between Mn and Fe and their influence on the poor separation of manganese and iron oxides. Simultaneously, the composite oxide $Mn_xFe_{3-x}O_4$ was synthesized from MnO_2 and Fe_2O_3 in an air atmosphere within a temperature range of 500-1400°C. However, the morphology and related reactions of $Mn_xFe_{3-x}O_4$ with different x values have not been determined. Numerous techniques have proven effective in generating manganese ferrite nanoparticles that meet the specified dimensions and aesthetics. Nevertheless, their implementation in large-scale applications is hindered by the substantial expenses linked to the raw materials utilized, the elevated temperature necessary for the reaction, and the intricate nature of the process. Therefore, seeking a simpler and more efficient manganese ferrite preparation process has become a breakthrough point. The synthesis and characterization of micron-sized spherical $MnFe_2O_4$ by the oxidization process has been regarded as the most cost-effective and commonly employed method to synthesize manganese ferrite.

In this work, a new melting oxidation roasting technique is reported to further understand the interface reaction and formation mechanism of manganese ferrite ($MnFe_2O_4$) nanostructures. This study aims to bridge the existing knowledge gap by deeply studying the oxidation shape and interfacial reactions of MnO-Fe_2O_3 in an air atmosphere at different temperature, durations and molar ratios. Furthermore, the phase transition process of the MnO-Fe_2O_3 systems during $MnFe_2O_4$ formation and the phase composition and morphology evolution of Mn were measured via XRD, VSM, XPS, BET and SEM/EDS analyses. Given these findings, this technology has the potential to be adapted for the production of other significant spinel ferrite particles.

2. Experimental materials and methods

2.1. Raw materials

The tested MnO and Fe_2O_3 powders were chemical grade solvents and were utilized without additional purification. MnO and Fe_2O_3 were 99.9 wt.% pure. A TopSizer Intelligent Laser Particle Size Analyzer was used to examine the granulometric distributions of the Fe_2O_3 and MnO powders, revealing average particle sizes of 45.6 μm and 19.8 μm, respectively.

2.2. Synthesis procedure

In this study, micron-sized spherical manganese ferrite ($MnFe_2O_4$) was prepared via an oxidation method. A detailed flow chart of the experiment is shown in Fig. 1. First, the MnO and Fe_2O_3 powders with different Mn/Fe molar ratios were mixed homogeneously, and then, the mixtures were compressed by a mold to form cylindrical briquettes at a pressure of 20 MPa (size: 10×10 mm). The oxidization roasting experiment was subsequently performed in a high-temperature tube furnace under an air atmosphere. The tube furnace was ramped up to the designated temperature at a rate of 8°C/min. The roasting process occurred within a specific temperature range (1000-1400°C, with a temperature difference of 100°C) and time range (10-50 min, with a time difference of 10 min), and the mixtures were placed in a heat-resistant corundum crucible. Notably, the mixture sample should be placed on the back of the corundum crucible

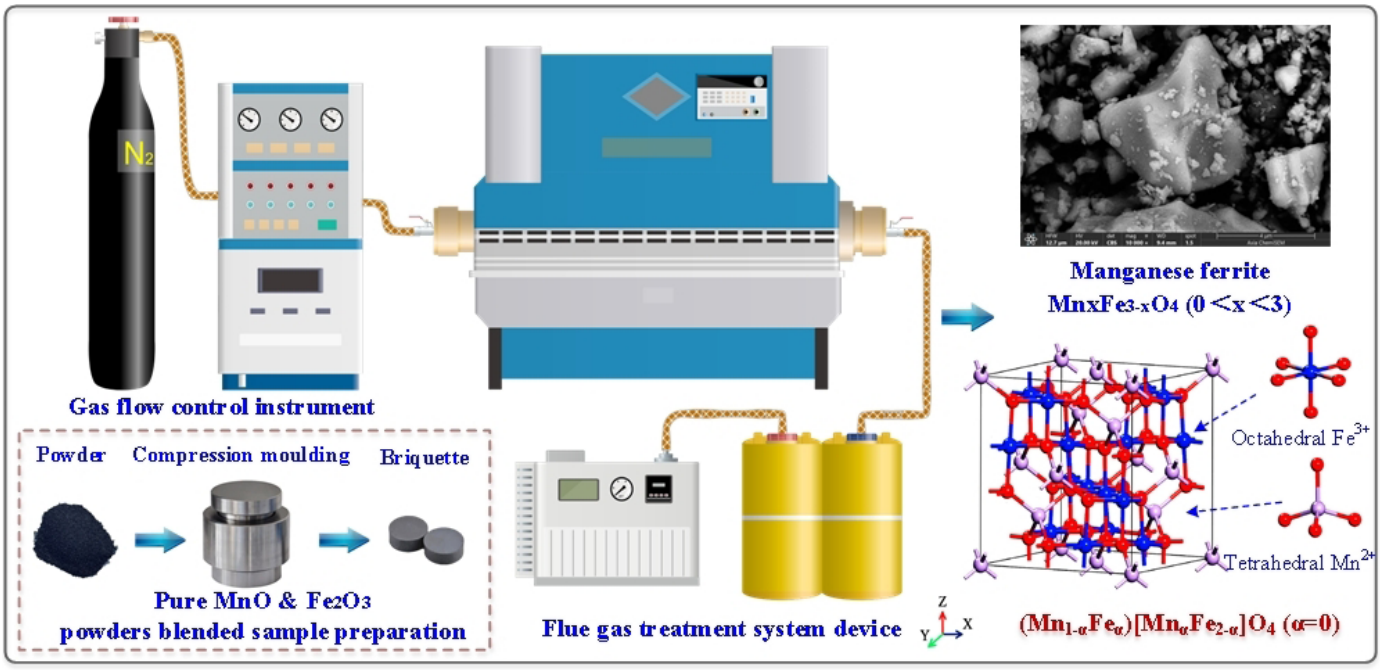

Fig. 1. Schematic diagram of the preparation of the manganese ferrite $Mn_xFe_{3-x}O_4$ samples by oxidation roasting technology

so that the bulging air can be fully exposed to the test sample for better oxidation and then positioned centrally within the furnace chamber for roasting. After being roasted at a given temperature, the samples were placed on the ground and cooled to room temperature in an air atmosphere for the subsequent characterization tests. Details of the device have been reported in our previous studies [29-31].

2.3. Characterization methods

Notably, the roasted samples were first ground for 3 min in a sample grinder to pass through a 200-mesh sieve and then ground for 5 min in a ball mill to bring the samples into nanometer-sized particles for X-ray diffraction (XRD), X-ray photoelectron spectroscopy (XPS), vibrating sample magnetometry (VSM), and SEM measurements.

The phase composition of the roasted samples ($MnFe_2O_4$) was analyzed via a Bruker D8 diffractometer with the following parameter settings: radiation source, Cu Kα (l = 1.54156A°); tube current and voltage, 30 mA and 40 kV, respectively; and scanning area, 5-90°; and scanning rate, 8°/min. Ultimately, X' Pert High Score Plus was employed to analyze the data derived from the experiments and subsequently to create graphical representations.

The surface characteristics of micron-sized spherical manganese ferrate particles, including their constituent elements, chemical valence states, and atomic compositions of manganese (Mn) and iron (Fe), can be analyzed via X-ray photoelectron spectroscopy (XPS, Thermo Fisher Scientific K-Alpha). XPS detects the energy of the hit electrons by irradiating the surface of a sample with monochromatic X-rays generated from an aluminum target. The analysis typically reaches a depth of approximately 10 nm. The complete spectrum is predominantly utilized for qualitative assessments, involving relatively large increments for parameter adjustments, and serves to swiftly ascertain the various elements present on the surface of the sample. The XPS data were analyzed via XPS peak 4.1 software, and the surface areas of the peaks represented the relative contents of the surface elements.

On the basis of the adsorption characteristics of nitrogen on the material surface, the specific surface area and pore size distribution of the samples were determined via nitrogen adsorption methods. The surface structure of a sample can be examined by scanning electron microscopy (SEM). TEM characterization can be used to observe the structure and morphology of nanomaterials effectively. The content of Mn- or Fe-rich particles in the roasted $MnO\text{-}Fe_2O_3$ powders was determined via SEM–EDS analysis.

3. Results and discussion

3.1. Phase transformation

Fig. 2 shows the XRD patterns of various molar ratios of $MnFe_2O_4$ samples baked by the $MnO\text{-}Fe_2O_3$ system for 30 min at 1300°C under an air atmosphere. The characteristic diffraction peaks of the Fe_2O_3, Mn_3O_4 and spinel-type manganese ferrite phases are present mainly at Mn:Fe = 1:4, and when the ratio of Mn:Fe is altered from 1:4 to 2:4, an observable decrease in the intensity of the characteristic diffraction peaks of Fe_2O_3 occurs, whereas the intensity of the characteristic diffraction peaks of Mn_2O_3 decreases until it disappears entirely. Conversely, the intensity of the diffraction peaks corresponding to the manganese ferrate phase within the spinel structure increased and remained stable. Moreover, the characteristic diffraction peak (311)

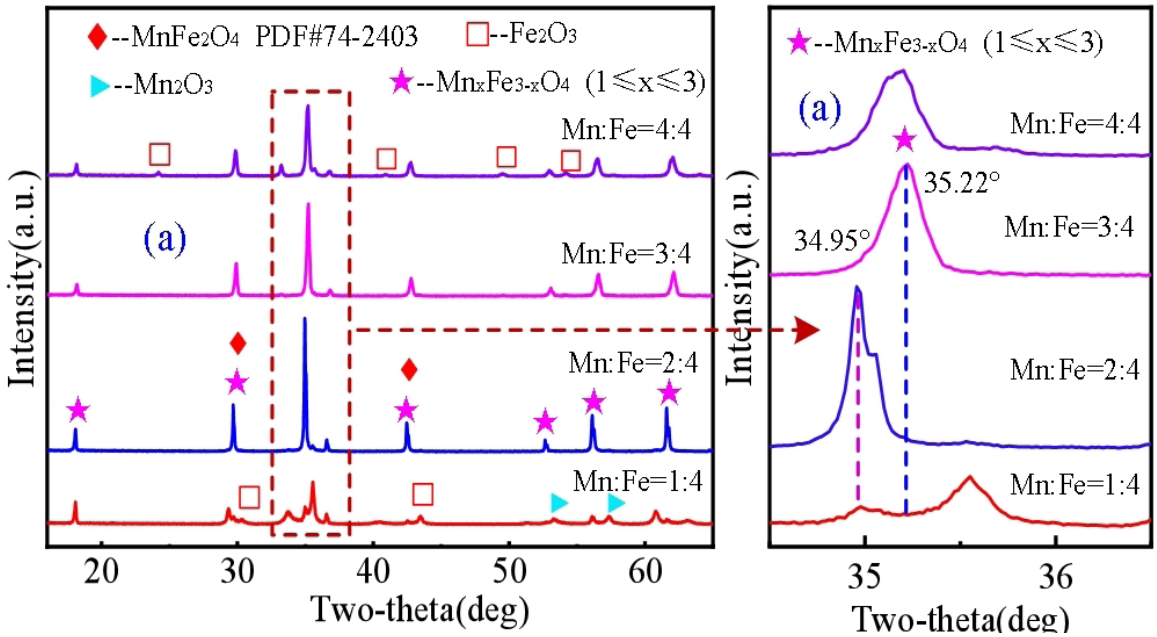

Fig. 2. XRD patterns of various molar ratio series of $MnFe_2O_4$ samples baked by the $MnO\text{-}Fe_2O_3$ system for 30 min at 1300°C under an air atmosphere

2θ value of $Mn_xFe_{3-x}O_4$ shifted from $FeMn_2O_4$ (2θ = 34.94°) to $MnFe_2O_4$ (2θ = 35.22°), suggesting that an optimal molar ratio facilitates the effective synthesis of both $FeMn_2O_4$ and $MnFe_2O_4$. When the molar ratio of Mn/Fe exceeded 2:4, the characteristic diffraction peak intensity of $Mn_xFe_{3-x}O_4$ was significantly reduced, and the XRD map also revealed excessive Fe_2O_3, which may have been oxidized to ferric oxide, leading to a decrease in the purity of the synthesized manganese ferrate sample.

Fig. 3 shows the XRD patterns of the $MnFe_2O_4$ samples of the MnO-Fe_2O_3 system roasted for 30 min under an air atmosphere with Mn:Fe = 1:2 in the temperature range of 1000~1400°C. Fig. 3(a) shows the XRD patterns of the samples at oxidization roasting temperature of 1000°C and 1400°C. The Mn_2O_3 diffraction peak disappeared, and the Fe_2O_3 diffraction peak weakened when the roasting temperature was increased from 1000°C to 1200°C. This is mainly because the oxidation of Mn^{2+} is preferred over that of Fe^{2+} in the crystal structure of $Mn_xFe_{3-x}O_4$. Moreover, in this temperature range, the characteristic diffraction peak intensity of $Mn_xFe_{3-x}O_4$ increased significantly with increasing oxidation roasting temperature from 1000°C to 1200°C and then stabilized again. Elevated temperature are beneficial for the formation of manganese ferrite because the Mn/Fe malar ratio at the surface is close to the theoretical stoichiometric ratio of 1:2. When the roasting temperature was increased from 1100°C to 1300°C, the characteristic diffraction peaks of $Mn_xFe_{3-x}O_4$ were stable, but the characteristic diffraction peak (311) with a primary intensity of 100% shifted from 2θ = 35.394° (Fe_3O_4, PDF#89-0688) to 2θ = 34.941° ($FeMn_2O_4$, PDF#75-0035). When the temperature reaches 1300°C, the main phases are only $Mn_xFe_{3-x}O_4$ and the unreacted Mn_2O_3 and Fe_2O_3, indicating the complete chemical combination of MnO and Fe_2O_3 at Mn:Fe = 1:2 for 30 min. When the oxidation roasting temperature increased from 1300°C to 1400°C, the characteristic diffraction peak of $Mn_xFe_{3-x}O_4$ detected by XRD gradually weakened with increasing oxidation roasting temperature, and the diffraction peak changed from a higher angle (2θ = 35.225°) to a lower angle (2θ = 34.916°). Together, the results indicate that neither lower nor higher temperature result in the formation of stable manganese ferrite.

Fig. 4 shows the XRD patterns of various $MnFe_2O_4$ samples obtained with the MnO-Fe_2O_3 system at a Mn:Fe ratio of 1:2 under an air atmosphere at 1300°C. No diffraction peaks of impurities were detected when the oxidation roasting duration exceeded 20 min, indicating that the synthesized $MnFe_2O_4$ remained stable under these conditions. The characteristic diffraction peaks of the spinel-type manganese ferrate samples in

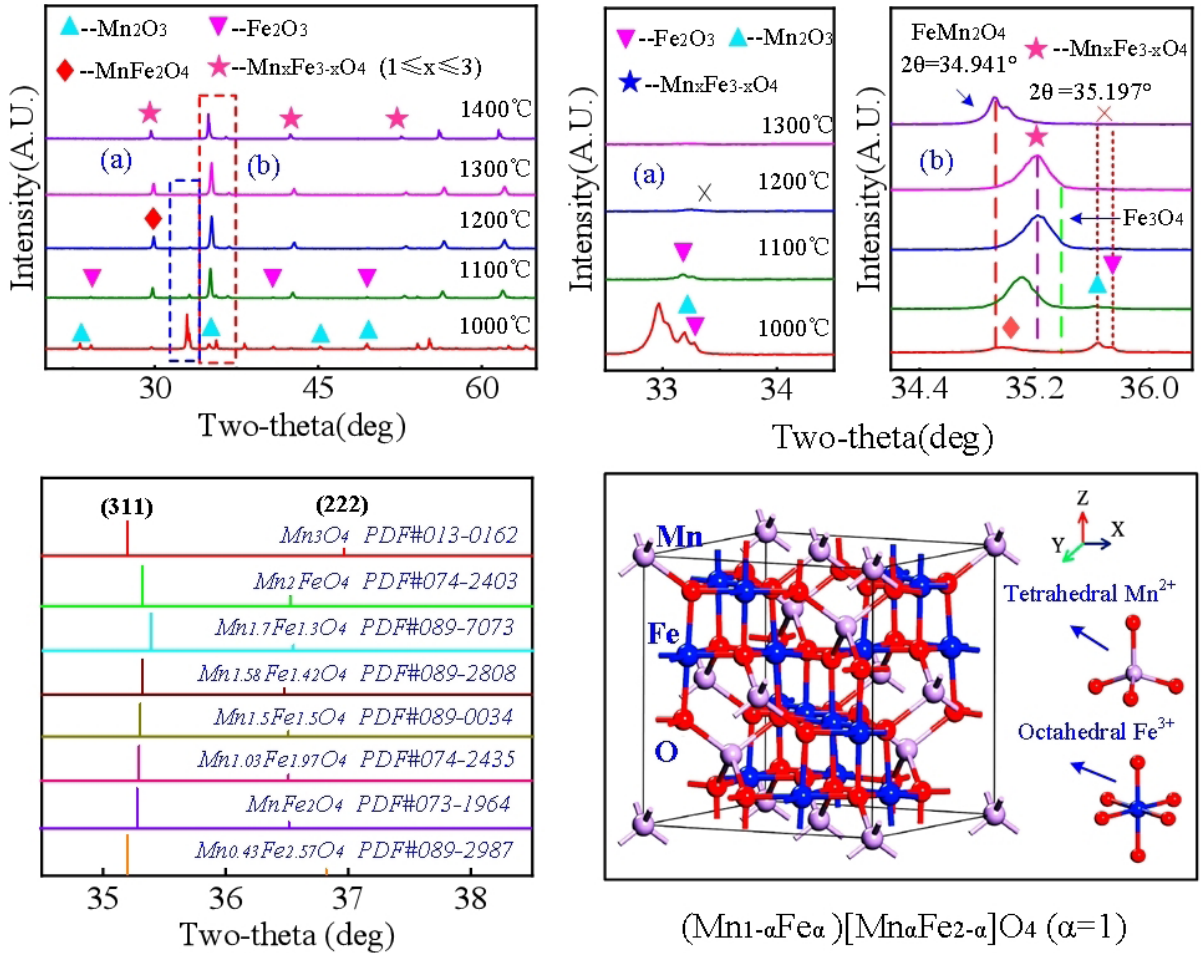

Fig. 3. XRD patterns of the $MnFe_2O_4$ samples of the MnO-Fe_2O_3 system roasted for 30 min in an air atmosphere at Mn:Fe = 1:2 in the temperature range of 1000~1400°C: (a) oxidation roasting temperature; (b) standard substance of the $Mn_xFe_{3-x}O_4$ group; (c) crystal structure of the normal spinel $MnFe_2O_4$

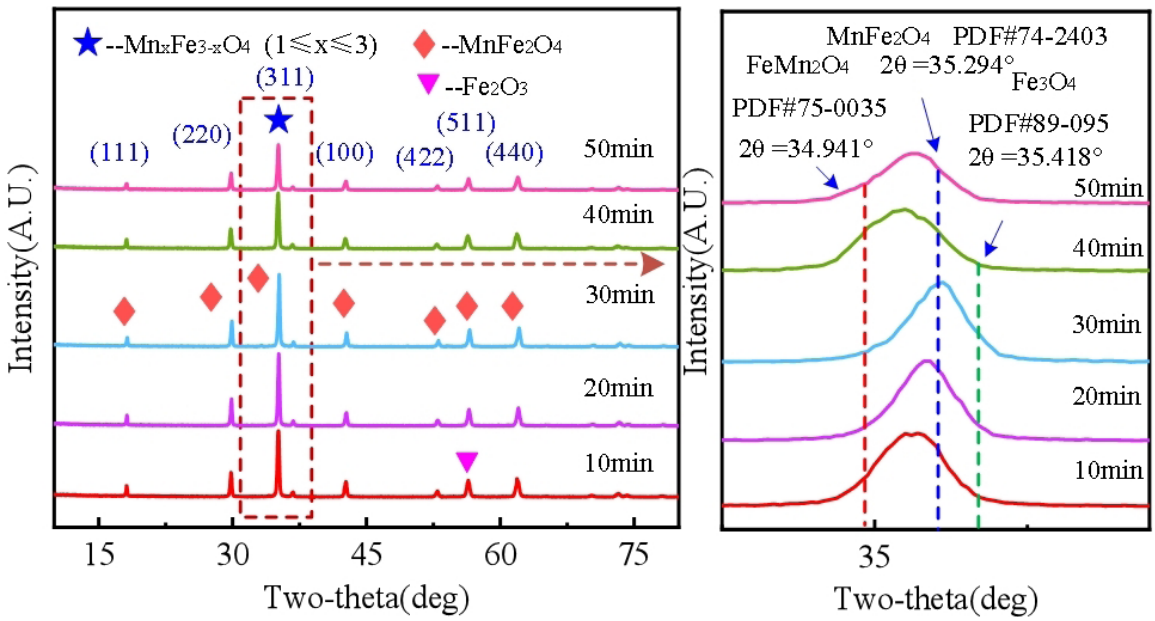

Fig. 4. XRD patterns of various $MnFe_2O_4$ samples produced by the MnO-Fe_2O_3 system at a Mn:Fe ratio of 1:2 under an air atmosphere at 1300°C

the 2θ range of 25~70 are in the order of (220), (311), (222), (400), (422), (511), and (400) crystal planes. Additionally, the crystal structure of spinel-type manganese ferrate is a cubic crystal system, and its crystalline formula is represented as $Mn^{2+}{}_8Fe^{3+}{}_{16}O^{2-}{}_{32}$.

3.2. X-ray photoelectron spectroscopy investigation

X-ray photoelectron spectroscopy (XPS) was employed to investigate the chemical properties of the manganese and iron in the spinel-type crystal structure on the surface of the spinel-type manganese ferrite products synthesized by oxidation roasting processes. Fig. 5 shows the XPS analysis of manganese ferrate ($Mn_xFe_{3-x}O_4$) synthesized at a temperature of 1300°C and heated at different molar ratios for 30 min. In the structural composition of spinel-type manganese ferrate, the Fe ions reside in tetrahedral and octahedral configurations within the spinel crystalline framework, establishing distinct chemical states and environments for both cations and anions. Iron ions (Fe^{2+} and Fe^{3+}) and manganese ions (Mn^{2+} and Mn^{3+}) exhibit varying binding energies across their distinct oxidation states. Therefore, the two spin–orbit coupled-state electrons ($Fe2p_{3/2}$, $Fe2p_{1/2}$, $Mn2p_{3/2}$, and $Mn2p_{1/2}$) exhibit distinct binding energies. The Fe2p spectrum

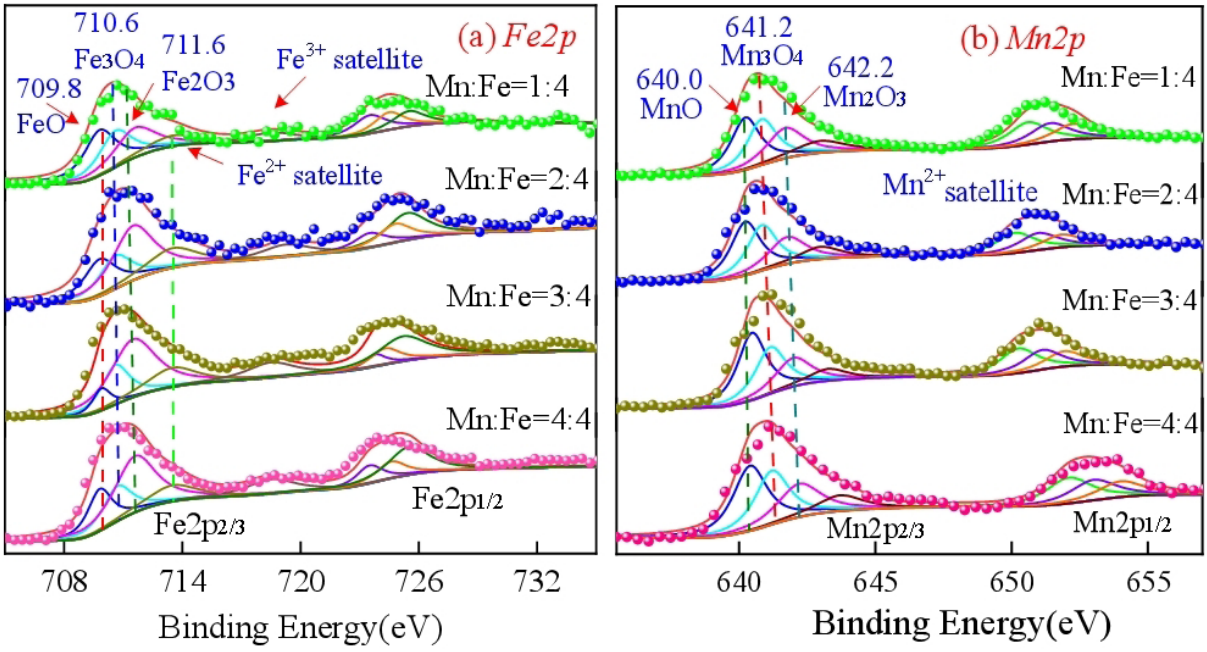

Fig. 5. X-ray photoelectron spectroscopy (XPS) of synthesized $Mn_xFe_{3-x}O_4$ samples roasted at 1300°C for 30 min with Mn/Fe molar ratios ranging from 1:4 to 2:4

of the roasting products is shown in Fig. 5(a). XPS peak 4.1 analysis indicates that the binding energies for the Fe2p3/2 orbitals in FeO, Fe_3O_4, and Fe_2O_3 are 709.8 eV, 710.6 eV, and 711.6 eV, respectively. Notably, a distinct FeO satellite peak in the binding energy range of 715-720 eV is observed in the Fe2p region, indicating the presence of Fe_3O_4 (Fe_2O_3-FeO) or FeO in the sample. The presence of satellite peaks is associated with the intricate interplay of electrons in the outer layer of atoms. The data depicted in Fig. 5(a) indicate that the integrated areas of the Fe 2p3/2 peaks for FeO and Fe_3O_4 at a Mn:Fe ratio of 1:4 to 2:4 decrease at binding energies of 709.8 eV and 710.6 eV, whereas the area corresponding to Fe_2O_3 increases at a binding energy of 711.6 eV. This shows that at Mn:Fe = 2:4, the proportion of Fe^{3+} at B increases, and the proportion of Fe^{2+} at A decreases. The Mn2p spectrum of the roasting products is shown in Fig. 5(b). XPS peak 4.1 analysis indicates that the binding energies for the $Mn2p_{3/2}$ orbitals in MnO, Mn_3O_4, and Mn_2O_3 are 640.0 eV, 641.2 eV, and 642.2 eV, respectively. In addition, satellite peaks were detected in the Mn 2p map, with a binding energy of 644.4 eV. The data illustrated in Fig. 5(b) indicate that as the molar ratio of Mn to Fe decreases from 1:4 to 2:4, the binding peak area of the Mn 2p3/2 orbital for MnO increases, whereas the binding peaks for Mn_3O_4 and Mn_2O_3 in the 2p3/2 orbital decrease. The primary reason for this is that Fe metal can significantly impede the conversion of Mn^{3+} to Mn^{2+} and that Mn^{3+} occupies the octahedral position more efficiently than Fe^{3+} in the spinel structure. It was demonstrated that the oxidation of divalent manganese to trivalent manganese occurred prior to the oxidation of divalent ferrum (Fe). The results of XRD and XPS provided additional validation for the synthesis of spinel manganese ferrate, establishing a foundation for its application and a technical prototype for its production by oxidation processes.

3.3. Specific surface area and porosity of the synthesized $Mn_xFe_{3-x}O_4$ samples

Fig. 6(a) illustrates the nitrogen adsorption–desorption isotherms of the $Mn_xFe_{3-x}O_4$ samples with different manganese/iron ratios at 77.35 K. The BET surface area and t-plot micropore area of the samples were derived through DFT computational modeling and are presented in Fig. 6(b). Owing to their comparatively large pore-specific surface area and pore volume, the $Mn_xFe_{3-x}O_4$ samples with a Mn:Fe ratio of 1:4 exhibit good nitrogen adsorption and resolution ability, as can be readily observed. The adsorption isotherm curve is closed, and the maximum adsorption amount at room temperature and pressure is 55.26 cm^3/g. When Mn:Fe = 2:4 is changed to Mn:Fe = 4:4, the nitrogen absorption detachment performance is clearly best when Mn:Fe = 2:4. The pore structure parameters of the $Mn_xFe_{3-x}O_4$ samples were also evaluated via the DFT model, as illustrated in Fig. 6(c) and Fig. 6(d). The SSA of $Mn_xFe_{3-x}O_4$ significantly decreased with

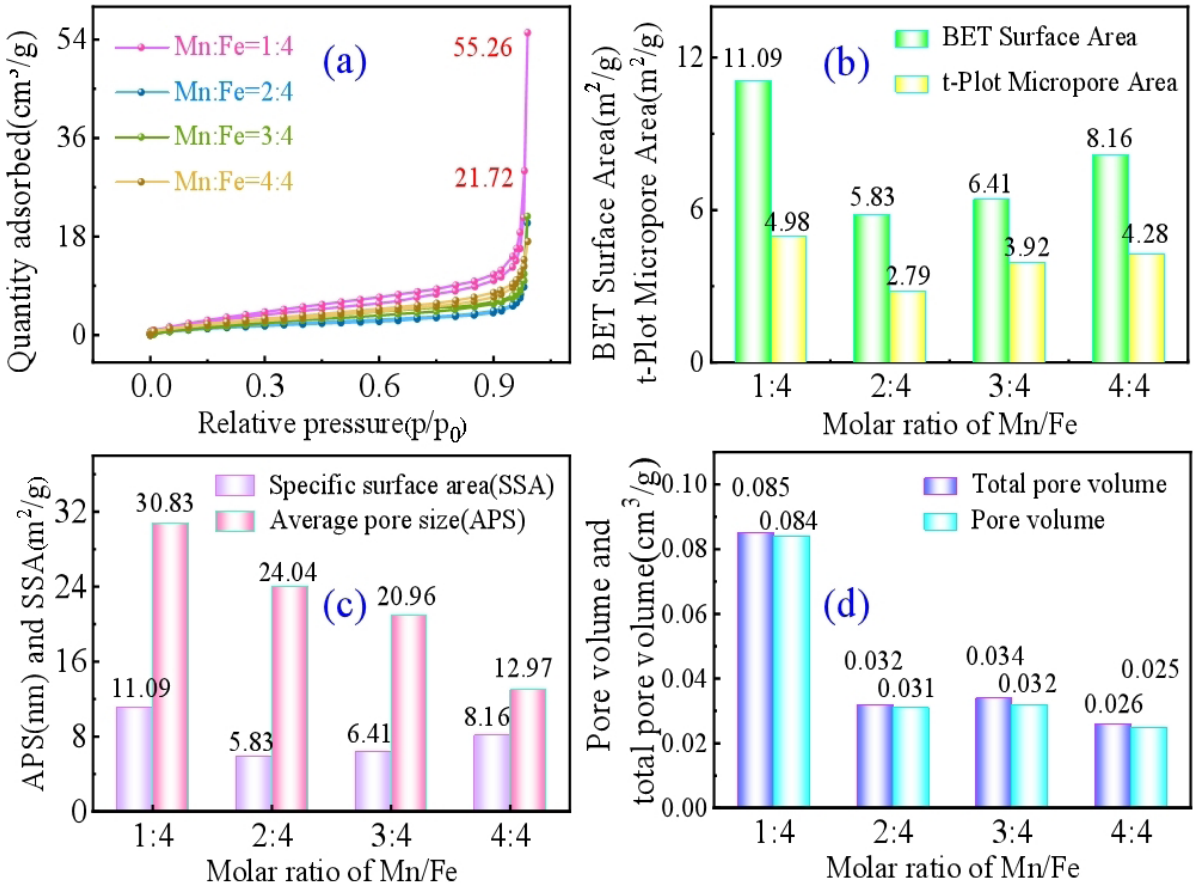

Fig. 6. N_2 adsorption–desorption isotherms of synthetic $Mn_xFe_{3-x}O_4$ samples roasted at a melting oxidization roasting temperature range of 1300°C for 30 min with a Mn/Fe molar ratio of 1:4 to 2:4 in an air atmosphere

decreasing Mn/Fe molar ratio from 1:0.5 to 1:3. As shown in Fig. 6(c), the SSA and APS of the $Mn_xFe_{3-x}O_4$ samples gradually transitioned from 5.83cm^3/g to 8.16cm^3/g and from 24.04 nm to 12.97 nm, respectively, as the Mn/Fe molar ratio decreased from 2:4 to 4:4. As shown in Fig. 6(d), the pore volume and total volume of the $Mn_xFe_{3-x}O_4$ samples gradually decreased from 0.085 cm^3/g to 0.032 cm^3/g and 0.084 cm^3/g to 0.031 cm^3/g with decreasing Mn/Fe molar ratios from 1:4 to 2:4, respectively. The pore volume and total volume of the $Mn_xFe_{3-x}O_4$ samples notably decreased to approximately 0.034 cm^3/g and 0.032 cm^3/g, respectively, when the molar ratio of Mn:Fe was less than 2:4. The increased pore volume and total pore volume index values of the samples are attributed primarily to the more efficient synthesis of the $Mn_xFe_{3-x}O_4$ phase at a reduced iron content, which consequently leads to an increased index of particle attributes.

3.4. Morphology investigation of the synthesized $Mn_xFe_{3-x}O_4$ samples

Fig. 7 depicts the microscopic structure of spinel manganese ferrite obtained by melting oxidation roasting technology. Fig. 7(a) shows the microstructure of the manganese ferrite particles synthesized at 1300°C for 30 min at a Mn:Fe ratio of 1:2. The reaction interfaces of the $Mn_xFe_{3-x}O_4$ samples were characterized and analyzed via optical microscopy and SEM–EDS. In the reaction system of MnO and Fe_2O_3, under the action of the raw material powder, the diffusion and oxidation reactions of iron and manganese make the particles and particles connect to form the iron–manganese wustite of block ore, which has a strong agglomeration trend. As shown in Fig. 7(a), the synthesized $Mn_xFe_{3-x}O_4$ samples have a small amount of sphere-like ferric oxide phase tightly wrapped on their surface because the rate of Mn^{2+} oxidation is faster than that of Fe^{2+}. This ultimately results in a much higher concentration of outer manganese ions in the manganese iron sample than internal manganese ions. Overall, the SEM images recorded at high magnification clearly show that the ceramic has uniform shapes and flat surfaces. The crystallinity and micromorphology of manganese ferrate differ with different methods. In the present study, the microscopic morphology of the manganese ferrate products obtained via different methods was octahedral, spherical, fibrous, or ceramic. Theoretically, the ratio of Mn, Fe, and O atoms in the synthesized $Mn_xFe_{3-x}O_4$ samples should be 1:2:4. According to the energy map analysis of spinel manganese ferrate in Fig. 7, the ratios of Mn, Fe, and O atoms in the synthesized $Mn_xFe_{3-x}O_4$ samples are 17.05%, 35%, and 47.95%, respectively. However, the actual atom ratio does not accord with the theoretical atom ratio. One reason is that Mn^{2+} ions prefer to produce Mn^{3+} ions in the synthesized $Mn_xFe_{3-x}O_4$ samples. Another reason is that the ratio of iron-manganese atoms in the wustite phase synthesized during the oxidation of the MnO-Fe_2O_3 system cannot be maintained at 2:1. This is also the primary reason for the synthesis of positive and anti-spinel manganese ferrite.

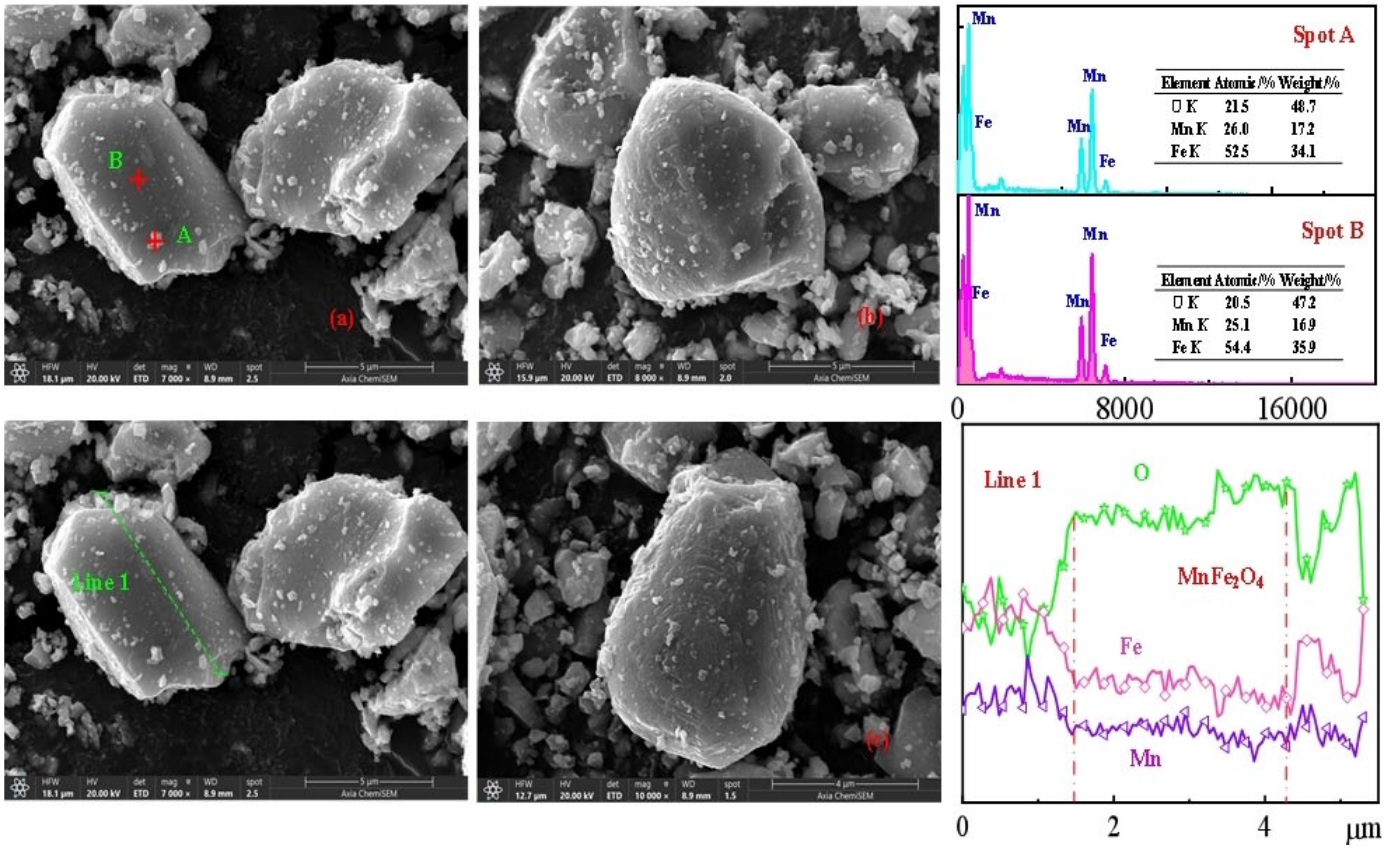

Fig. 7. SEM micrographs of fracture surfaces of the synthetic $Mn_xFe_{3-x}O_4$ samples roasted at a melting oxidization roasting temperature range of 1300°C for 30 min with a Mn/Fe molar ratio of 2:4 in an air atmosphere

3.5. Magnetic properties of the synthesized $Mn_xFe_{3-x}O_4$ samples

Fig. 8 demonstrates the magnetization hysteresis loops of various molar ratios of $MnFe_2O_4$ samples baked by the MnO-Fe_2O_3 system for 30 min under an air atmosphere at 1300°C, confirming the ferromagnetic characteristics of the samples. Fig. 8 clearly shows that the saturation magnetization of the synthesized micron-scale spherical manganese ferrite sample slowly decreases from 69.10 emu/g to 64.96 emu/g, and the saturation magnetization intensity of the samples significantly decreases from 64.96 emu/g to 36.15 emu/g with increasing Mn^{2+} content. The main cause of magneto-crystalline anisotropy in spinel-structured $Mn_xFe_{3-x}O_4$ samples is a consequence of the spin–orbit coupling properties between the octahedral and tetrahedral metal cations. Additionally, the coercivity (Hc) increased dramatically from 10.05 Oe to 91.14 Oe with increasing manganese content. Moreover, the ratio of saturation to residual magnetization intensity (Ms/Mr) also dramatically decreased from 6.33 to 2.11. In accordance with the XRD results, more impurities (Fe_2O_3) at a Mn:Fe ratio of 4:4 contributed to a decrease in the indicators of the samples. Early studies revealed that the maximum saturation magnetization of $Mn_xFe_{3-x}O_4$ samples with high purity was 71.8 emu/g. As the Mn content increased, the maximum saturation magnetization of the $Mn_xFe_{3-x}O_4$ samples significantly decreased, indicating the reduced purity of the synthetic sample. The test results are consistent with the XRD test results.

3.6. Reaction mechanism of the synthetic manganese ferrite $MnFe_2O_4$

According to the preceding detection and analysis, the reaction mechanism of the $MnFe_2O_4$ samples synthesized by melting and oxidation is shown in Fig. 9. Fig. 9(a) shows the reaction mechanism of the manganese ferrite samples by melting below 1200°C. In the initial stages (Eqs. (1-2)), divalent manganese is easier to oxidize to trivalent manganese than is divalent iron. The resulting Mn_2O_3 and Fe_2O_3 subsequently undergo a reaction to produce manganese ferrate, which possesses a spinel structure. In the second stage (Eqs. (3-5)), Mn^{2+} can directly undergo ion migration and exchange with Fe^{2+} in spinel Fe_3O_4 to generate spinel-type $Mn_xFe_{3-x}O_4$ because Mn_3O_4 ($[Mn^{3+}][Mn^{2+}Mn^{3+}]O_4$) has a similar spinel structure to Fe_3O_4 ($[Fe^{3+}][Fe^{2+}Fe^{3+}]O_4$). In other words, the tetrahedral coordinated Mn^{2+} ions in Mn_3O_4 with spinel-type crystal structures were replaced by tetrahedral coordinated Fe^{2+} ions to form $Mn_xFe_{3-x}O_4$ with a similar crystal structure. Notably, some of the substituted Mn^{2+} is prone to Fe^{2+} binding to form the wustite phase $Fe_yMn_{1-y}O$, which has a similar structure. In the third stage (Eqs. (6-8)), the wustite phase $Fe_yMn_{1-y}O$ can be oxidized to $Mn_xFe_{3-x}O_4$ ($0 \le x \le 1$) when the value of y is less than 0.33. In addition, the wustite phase $Mn_yFe_{1-y}O$ is easily oxidized into stable $MnFe_2O_4$ as the temperature increases. Simultaneously, Mn_3O_4 is prone to cracking to produce a manganese oxide phase and oxygen at high temperature, and the manganese ions readily infiltrate the crystal lattice of iron trioxide. The final stage involves the

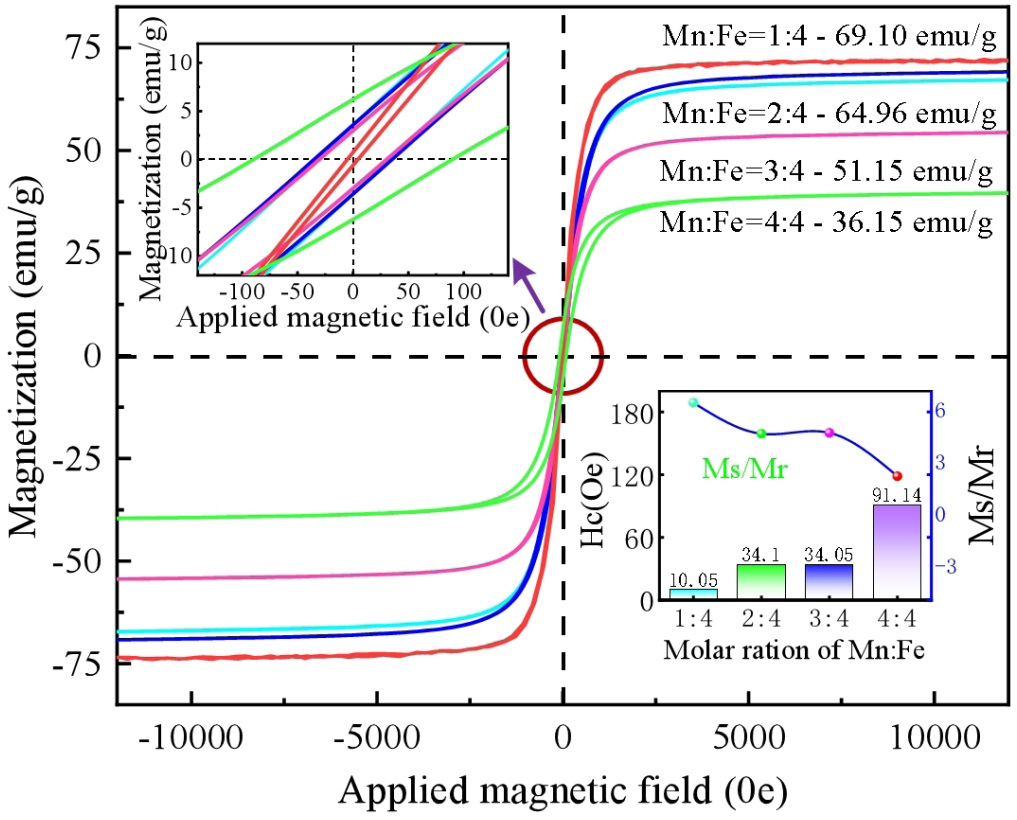

Fig. 8. Magnetization hysteresis loops of synthetic $Mn_xFe_{3-x}O_4$ samples roasted at a melting oxidization roasting temperature range of 1300°C for 30 min with a Mn/Fe molar ratio of 1:4 to 2:4 in an air atmosphere

interconversion of both the positive and reverse spinel structures (Eq. (9)). As the temperature increased, $Mn_xFe_{3-x}O_4$ exhibited positive and anti-spinel structures, where the metal cations, Mn^{2+} and Fe^{3+}, are positioned at the A (tetrahedral) and B (octahedral) sites, respectively [32]. These sites are created through a face-centered cubic packing arrangement of oxygen anions, represented as $[Mn_{1-\alpha}{}^{2+}Fe_{\alpha}{}^{3+}]_{tet.}\,[Mn_{\alpha}{}^{2+}Fe_{2-\alpha}{}^{3+}]_{oct.}\,O_4$ (α is the degree of inversion of Mn, $0 \le x \le 1$). In normal spinel ($\alpha = 0$), Mn^{2+} occupies the A position, whereas manganese ferrate has a spinel-type crystalline structure. In inverse spinel ($\alpha = 1$), all of the Mn^{3+} ions enter the B position and exhibit an anti-spinel type structure ($[Fe^{2+}]_{tet.}[Mn^{3+}Fe^{3+}]_{oct.}O_4$). The change in the α value is associated with the oxidation of Mn^{2+} during the synthesis of manganese ferrate. The newly formed Mn^{3+} will occupy all the B positions, whereas some of the Fe^{3+} in the B positions will undergo partial reduction to Fe^{2+} to preserve the electrical properties, structural integrity, and stability [33].

$$6MnO + O_2 = 2Mn_3O_4 \quad (1)$$

$$6[Mn^{2+}]O + O_2 = 2[Mn^{3+}][Mn^{2+}Mn^{3+}]O_4 \quad (2)$$

$$Fe_3O_4 + Mn_3O_4 \rightarrow Mn_xFe_{3-x}O_4\ (0 < x < 3) \quad (3)$$

$$[Fe^{3+}][Fe^{2+}Fe^{3+}]O_4 + 2[Mn^{3+}]\,[Mn^{2+}Mn^{3+}]O_4 \rightarrow$$
$$\rightarrow [Mn^{2+}Fe^{2+}]_x[Mn^{3+}Mn^{3+}]_{3-x}O_4(0 < x < 3) \quad (4)$$

$$y[Fe^{2+}][O^{2-}] + 1 - y[Mn^{2+}][O^{2-}] =$$
$$= [Fe^{2+}]_y[Mn^{2+}]_{1-y}[O^{2-}]_4 \quad (5)$$

$$Fe_yMn_{1-y}O(0 < y < 0.33) + O_2 \rightarrow$$
$$\rightarrow Mn_xFe_{3-x}O_4(0 < x < 1) \quad (6)$$

$$Fe_yMn_{1-y}O\ (0 \le y \le 1) + O_2 \rightarrow$$
$$\rightarrow Mn_xFe_{3-x}O_4\ (1 < x \le 3) +$$
$$+ Mn_yFe_{1-y}O\ (0 < y < 0.33) + Fe_xO\ (x < 1) \quad (7)$$

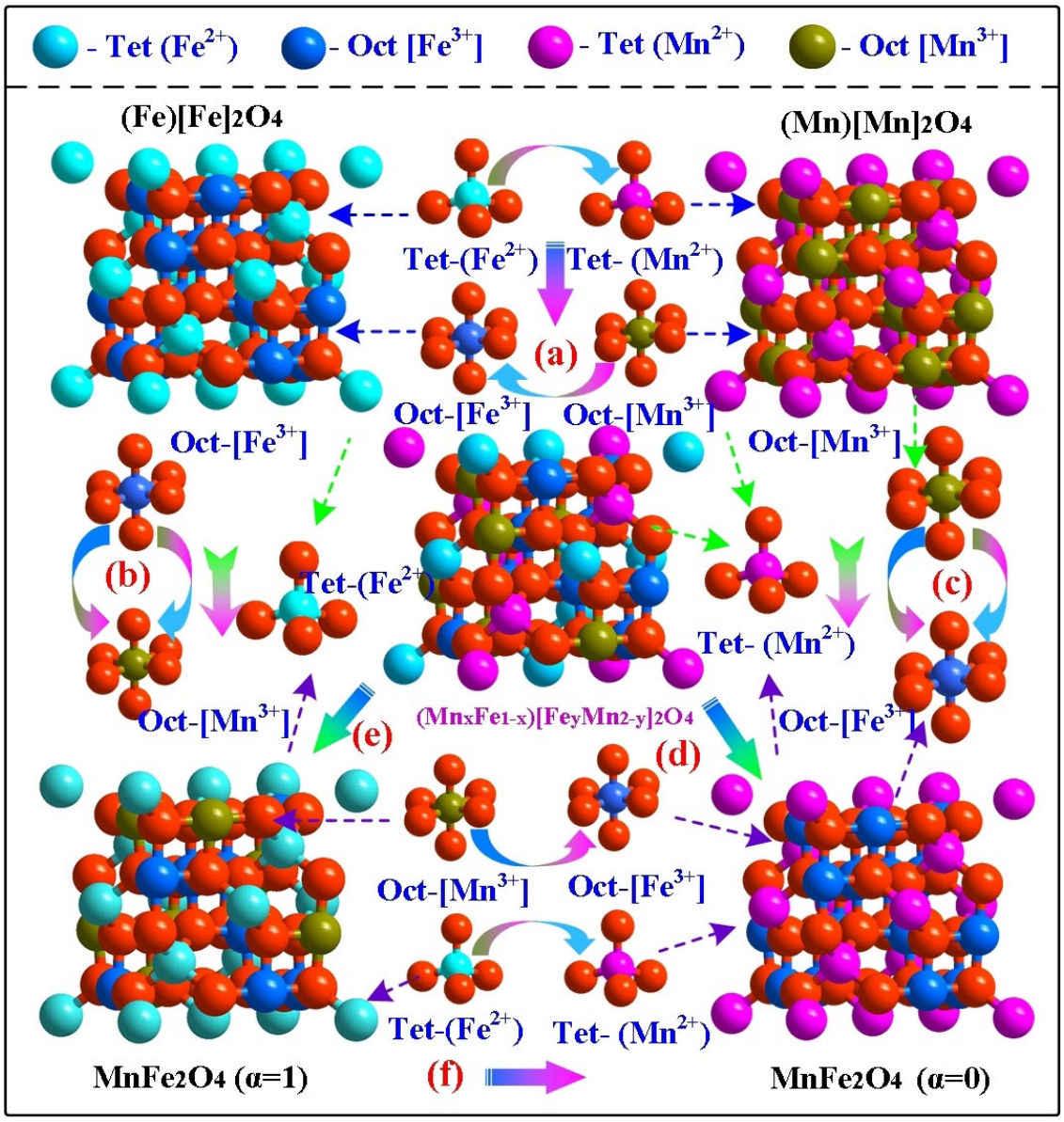

Fig. 9. Schematic diagram of the reaction mechanism and oxidization behaviors in the synthesis process of the $MnFe_2O_4$ samples by oxidation roasting technology

$$[Fe^{3+}]_2O_3 + [Mn^{3+}][Mn^{2+}Mn^{3+}]O_4 \rightarrow$$
$$\rightarrow [Mn^{2+}Fe^{2+}]_x[Mn^{3+}Mn^{3+}]_{3+x}O_4\ (0 < x < 3) + O_2 \quad (8)$$

$$(Mn_{1-\alpha}Fe_\alpha)_{tet.}\ [Mn_\alpha Fe_{2-\alpha}]_{oct.}O_4\ (\alpha = 0) \leftrightarrow$$
$$\leftrightarrow (Mn_{1-\alpha}Fe_\alpha)_{tet.}\ [Mn_\alpha Fe_{2-\alpha}]_{oct.}\ O_4\ (0 < \alpha \leq 1) \quad (9)$$

4. Conclusions

In summary, this research advances of manganese ferrite ($MnFe_2O_4$) using oxidization roasting process from Mn_2O_3 and Fe_2O_3 systems and has valuable implications for Spinel-type catalysts. During the synthesis of manganese ferrate, the XRD and SEM results revealed that the spinel $MnFe_2O_4$ microparticles were successfully synthesized from the MnO and Fe_2O_3 systems at a Mn:Fe ratio of 1:2 when the roasting temperature was 1300°C and the roasting time was 30 min. As the roasting temperature increases, the tetrahedral site (A) transitions to the octahedral site (B), resulting in a greater proportion of the positive spinel phase. However, the purity of synthetic manganese ferrite decreased when the temperature was above 1300°C, indicating that the x value of manganese ferrite gradually decreased from 1.

The morphological characteristics and property development of spinel manganese ferrite were investigated through SEM/EDS, XRD, XPS, and BET analytical techniques. When the Mn:Fe ratio reached 1:2, the synthesized $Mn_xFe_{3-x}O_4$ samples presented a total pore volume of 0.034 cm^3/g, a pore volume of 0.032 cm^3/g, an SSA of 6.41cm^3/g and an APS of 2.96 nm. According to the above data, the positive spinel structure and anti-spinel structure of the $Mn_xFe_{3-x}O_4$ samples are bound to exist and transform together in the process of synthesizing manganese ferrate by melting oxidation roasting technology. In summary, this research not only advances the theoretical understanding but also provides practical insights that can be leveraged in the synthesis of $Mn_xFe_{3-x}O_4$ by melting oxidation roasting technology.

Acknowledgments

The authors received financial support from the National Natural Science Foundation of China (52104332, 52374339) and the Doctoral Research Foundation of Liaoning Province, China (2023-BS- 171).

REFERENCES

[1] H. El Moussaoui, T. Mahfoud, S. Habouti, et al., Synthesis and magnetic properties of tin spinel ferrites doped manganese. J. Magn. Magn. Mater. **405**, 181-186 (2016). DOI: https://doi.org/10.1016/j.jmmm.2015.12.059

[2] R. Masrour, M. Hamedoun, A Benyoussef, Magnetic properties of $MnCr_2O_4$ nanoparticle. J. Magn. Magn. Mater. **322** (3), 301-304 (2010). DOI: https://doi.org/10.1016/j.jmmm.2009.08.051

[3] D. Carta, A. Corrias, G. Navarra, A total X-ray scattering study of $MnFe_2O_4$ nanoparticles dispersed in a silica aerogel matrix. J. Non-Cryst. Solids: X **357** (14), 2600-2603 (2011).

[4] M.A. Willard, Y. Nakamura, D.E .Laughlin, et al., Magnetic properties of ordered and disordered spinel-phase ferrimagnets. J. Am. Ceram. Soc. **82** (12), 3342-3346 (1999).

[5] M. Stoia, E. Muntean, C. Păcurariu, et al., Thermal behavior of $MnFe_2O_4$ and $MnFe_2O_4$/C nanocomposite synthesized by a solvothermal method. Thermochim. Acta. **652**, 1-8 (2017).

[6] X. Lin, X. Lv, L. Wang, et al., Preparation and characterization of $MnFe_2O_4$ in the solvothermal process: their magnetism and electrochemical properties. Mater. Res. Bull. **48** (7), 2511-2516 (2013).

[7] X. Wu, Z. Ding, W. Wang, et al., Effect of polyacrylic acid addition on structure, magnetic and adsorption properties of manganese ferrite nanoparticles. Powder Technol. **295**, 59-68 (2016).

[8] E.E. Carpenter, C.J. O'Connor, V.G. Harris, Atomic structure and magnetic properties of $MnFe_2O_4$ nanoparticles produced by reverse micelle synthesis. J. Appl. Phys. **85** (8), 5175-5177 (1999).

[9] M.M. Rashad, R.M. Mohamed, M.A. Ibrahim, et al., Magnetic and catalytic properties of cubic copper ferrite nanopowders synthesized from secondary resources. Adv. Powder Technol. **23** (3), 315-323 (2012).

[10] D. Chen, Y. Zhang, Z. Kang, A low temperature synthesis of $MnFe_2O_4$ nanocrystals by microwave-assisted ball-milling. Chem. Eng. J. **215**, 235-239 (2013). DOI: https://doi.org/10.1016/j.cej.2012.10.061

[11] J. Ding, P.G. McCormick, R. Street, Formation of spinel Mn-ferrite during mechanical alloying. J. Magn. Magn. Mater. **171** (3), 309-314 (1997). DOI: https://doi.org/10.1016/S0304-8853(97)00093-0

[12] M.P. Reddy, A.M.A. Mohamed, M.V. Ramana, et al., Spark plasma sintering and microwave electromagnetic properties of $MnFe_2O_4$ ceramics. J. Magn. Magn. Mater. **395**, 185-189 (2015).

[13] B. Aslibeiki, P. Kameli, Magnetic properties of $MnFe_2O_4$ nano-aggregates dispersed in paraffin wax. J. Magn. Magn. Mater. **385**, 308-312 (2015). DOI: https://doi.org/10.1016/j.jmmm.2015.03.023

[14] Y. Zhang, B. Liu, Z. You, et al., Consolidation behavior of high-Fe manganese ore sinters with natural basicity. Miner. Process. Extr. Metall. Rev. **37** (5), 333-341 (2016). DOI: https://doi.org/10.1080/08827508.2016.1218870

[15] M.M. Rashad, Synthesis and magnetic properties of manganese ferrite from low grade manganese ore. Materials Science and Engineering: B. **127** (2-3), 123-129 (2006).

[16] B. Liu, Y. Zhang, J. Wang, et al., Investigations on the MnO_2-Fe_2O_3 system roasted in air atmosphere. Adv. Powder Technol. **28** (9), 2167-2176 (2017). DOI: https://doi.org/10.1016/j.apt.2017.05.023

[17] L. Gao, Z. Liu, Y. Ge, et al., Synthesis and characterization of manganese ferrite $Mn_xFe_{3-x}O_4$ from ferruginous manganese ores by multi-step roasting and magnetic separation. Powder Technol. **356**, 373-382 (2019).

[18] B. Liu, Y. Zhang, J. Wang, et al., A further investigation on the MnO_2-Fe_2O_3 system roasted under CO-CO_2 atmosphere. Adv. Powder Technol. **30** (2), 302-310 (2019).
DOI: https://doi.org/10.1016/j.apt.2018.11.006

[19] J. Ding, P.G. McCormick, R. Street, Formation of spinel Mn-ferrite during mechanical alloying. J. Magn. Magn. Mater. **171** (3), 309-314 (1997).
DOI: https://doi.org/10.1016/S0304-8853(97)00093-0

[20] F. Toolenaar, M.T.J. Van Lierop-Verhees, Reactive sintering of manganese ferrite. J. Mater. Sci. **24**, 402-408 (1989).

[21] N.A.M. Deraz, G.A. El-Shobaky, Solid–solid interaction between ferric oxide and manganese carbonate as influenced by lithium oxide do. Thermochim. Acta. **375** (1-2), 137-145 (2001).

[22] M. Yue, J. Wang, Y. Han, et al., Degradation of bisphenol A by peroxymonosulfate activated by $MnFe_2O_4$ prepared by salt-assisted solution combustion synthesis. CIESC Journal. **71** (12), 5589 (2020).

[23] J.W. Long, M.S. Logan, E.E. Carpenter, et al., Synthesis and characterization of Mn–FeO_x aerogels with magnetic properties. J. Non-Cryst. Solids. **350**, 182-188 (2004).
DOI: https://doi.org/10.1016/j.jnoncrysol.2004.06.036

[24] J. Amighian, M. Mozaffari, B. Nasr, Preparation of nano-sized manganese ferrite ($MnFe_2O_4$) via coprecipitation method. Phys Status Solidi C. **3** (9), 3188-3192 (2006).
DOI: https://doi.org/10.1002/pssc.200567054

[25] V.M. Burojeanu, L. Fournes, A. Wattiaux, et al., Cation distribution and magnetic properties of manganese ferrite powder prepared by coprecipitation from MnO_2 and $FeSO_4 \cdot 7H_2O$. Int. J. Inorg. Mater. **3** (6), 525-529 (2001).
DOI: https://doi.org/10.1016/s1466-6049(01)00059-9

[26] Y. Gao, Prereduction and magnetic separation of low grade manganese ore. The University of Utah. (2011).

[27] M. Stoia, E. Muntean, C. Păcurariu, et al., Thermal behavior of $MnFe_2O_4$ and $MnFe_2O_4$/C nanocomposite synthesized by a solvothermal method. Thermochim. Acta. **652**, 1-8 (2017).

[28] Y.M.Z. Ahmed, Synthesis of manganese ferrite from non-standard raw materials using ceramic technique. Ceram. Int. **36** (3), 969-977 (2010).
DOI: https://doi.org/10.1016/j.ceramint.2009.11.020

[29] Z. Wang, H. Chen, X. Han, et al., Preparation and characterization of $MnFe_2O_4$ by a microwave-assisted oxidative roasting process. Adv. Powder Technol. **34** (7), 104040 (2023).

[30] L. Gao, P. Liu, W. Zhan, et al., New understanding on formation mechanism of $CaFe_2O_4$ in Fe_2O_3-Fe_3O_4-CaO-SiO_2 system during sintering Process: Phase transformation and morphologies evolution. Adv. Powder Technol. **33** (10), 103712 (2022).
DOI: https://doi.org/10.1016/j.apt.2022.103712

[31] S. Shi, L. Gao, J. Zhang, et al., New insights on consolidation behavior of Fe_2O_3 in the Fe_3O_4-CaO-MgO-SiO_2 system for fluxed pellet production: Phase transformations and morphology evolution. Miner. Eng. **214**, 108797 (2024).
DOI: https://doi.org/10.1016/j.mineng.2024.108797

[32] N. Akhlaghi, G. Najafpour-Darzi, Manganese ferrite ($MnFe_2O_4$) Nanoparticles: From synthesis to application – A review. J. Ind. Eng. Chem. **103**, 292-304 (2021).
DOI: https://doi.org/10.1016/j.jiec.2021.07.043

[33] K. Vamvakidis, M. Katsikini, D. Sakellari, et al., Reducing the inversion degree of $MnFe_2O_4$ nanoparticles through synthesis to enhance magnetization: evaluation of their 1 H NMR relaxation and heating efficiency. Dalton Trans. **43** (33), 12754-12765 (2014).